



Pushing the boundaries
of chemistry?
It takes
#HumanChemistry

Make your curiosity and talent as a chemist matter to the world with a specialty chemicals leader. Together, we combine cutting-edge science with engineering expertise to create solutions that answer real-world problems. Find out how our approach to technology creates more opportunities for growth, and see what chemistry can do for you at:

[evonik.com/career](https://www.evonik.com/career)



Compositional Patterning in Carbon Implanted Titania Nanotubes

Astrid Kupferer,* Alexander Holm, Andriy Lotnyk, Stephan Mändl, and Stefan G. Mayr*

Ranging from novel solar cells to smart biosensors, titania nanotube arrays constitute a highly functional material for various applications. A promising route to modify material characteristics while preserving the amorphous nanotube structure is present when applying low-energy ion implantation. In this study, the interplay of phenomenological effects observed upon implantation of low fluences in the unique 3D structure is reported: sputtering versus readsorption and plastic flow, amorphization versus crystallization and compositional patterning. Patterning within the oxygen and carbon subsystem is revealed using transmission electron microscopy. By applying a Cahn–Hilliard approach within the framework of driven alloys, characteristic length scales are derived and it is demonstrated that compositional patterning is expected on free enthalpy grounds, as predicted by density functional theory based *ab initio* calculations. Hence, an attractive material with increased conductivity for advanced devices is provided.

1. Introduction

Titania nanotube (NT) arrays are a highly versatile and customizable material mainly used in photocatalysis, solar cells, and biomedical engineering.^[1–4] The broad application spectrum can be attributed to TiO₂'s enhanced surface area in the nanotubular morphology. Additionally, self-organized synthesis using electrochemical anodization allows a precise adjustment of surface properties. This can be done by adapting the production voltage,

A. Kupferer
Research Group Biotechnology and Biomedicine, Peter Debye Institute for Soft Matter Physics
Leipzig University
Linnéstraße 5, 04103 Leipzig, Germany

A. Kupferer, A. Holm, Dr. A. Lotnyk, Dr. S. Mändl, Prof. S. G. Mayr
Leibniz Institute of Surface Engineering (IOM)
Permoserstraße 15, 04318 Leipzig, Germany
E-mail: astrid.kupferer@iom-leipzig.de; stefan.mayr@iom-leipzig.de

A. Kupferer, A. Holm, Prof. S. G. Mayr
Division of Surface Physics, Felix Bloch Institute for Solid State Physics
Leipzig University
Linnéstraße 5, 04103 Leipzig, Germany

 The ORCID identification number(s) for the author(s) of this article can be found under <https://doi.org/10.1002/adfm.202104250>.

© 2021 The Authors. Advanced Functional Materials published by Wiley-VCH GmbH. This is an open access article under the terms of the Creative Commons Attribution-NonCommercial-NoDerivs License, which permits use and distribution in any medium, provided the original work is properly cited, the use is non-commercial and no modifications or adaptations are made.

DOI: 10.1002/adfm.202104250

immersion time, and electrolyte composition. Moreover, the NT dimensions can be fine-tuned to provide application-specific diameters and heights. The standardized use of organic electrolytes supplemented with ammonium fluoride results in the incorporation of fluorine and carbon atoms into the NT arrays.^[5] However, we observe an exceptional biocompatibility, as proven in pioneering long-term cultures of sensitive adult tissues.^[6–8] Hence, anodically self-grown titania NT initially constitute a complex material with a high level of natural impurities.

To further enhance applicability and functionality of titania NT arrays, various routes are commonly followed. Changing the pristine amorphous phase to a crystalline one (anatase or rutile), for example, using a high temperature treatment,

results in the photocatalytic activity raising by 1–2 orders of magnitude.^[9–11] Moreover, the decoration of NT walls with nanoparticles enables, for instance, the design of highly efficient batteries and biosensors.^[12,13] Besides these procedures, band gap engineering opens up numerous possibilities to specifically alter electronic structure and optical properties. In particular, doping with the nonmetals carbon and nitrogen proves to be beneficial. Nitrogen doping remarkably increased the photocatalytic activity and shifted the band gap into visible light regions. Either done globally, for instance via a high-temperature treatment,^[14] or locally to establish distinct doped regions, as obtained by ion implantation.^[15,16] Alternatively, global carbon doping realized with high-temperature CO gas annealing provided excellent photocatalytic water splitting efficiencies^[17] and lower band gaps. Hence, when associated with the introduction of dopants and defects, a striking variety of surface colors with interconnected reactivity can be obtained: ranging from black to blue, green and red.^[18] Especially black TiO₂ has attracted attention for photocatalysis and wastewater treatment, due to its high density of oxygen vacancies in surface-near regions.^[19–21]

However, the exceptional hexagonal NT topography paired with naturally abundant impurities in the pristine amorphous phase constitutes a rather complex system compared to pure TiO₂ films or nanoparticles. As a consequence, thorough experimental and theoretical studies of ion implantation as a precisely tunable doping procedure of titania NT are rare.

In this study, we report on the selective manipulation of the local elemental distribution in NT arrays utilizing carbon implantation. We combine high-resolution transmission electron microscopy (TEM), density functional theory (DFT)

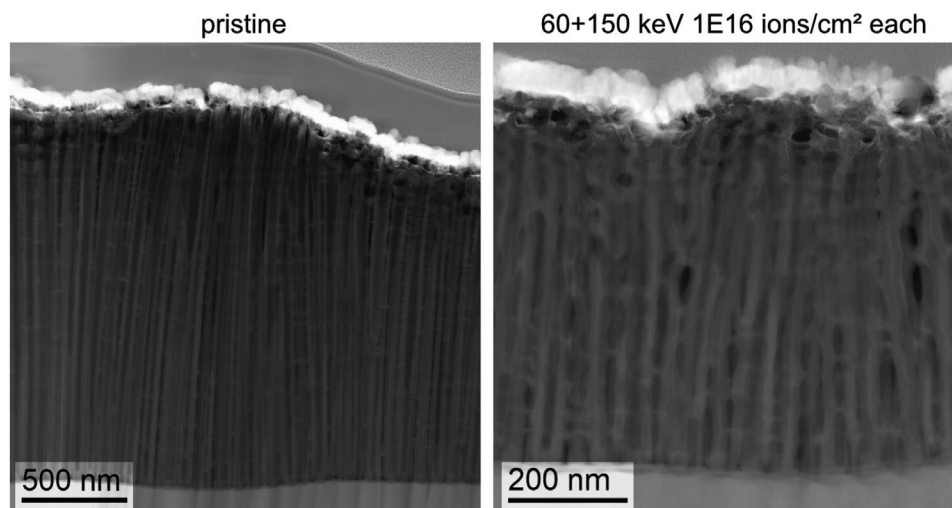


Figure 1. Scanning electron transmission microscopy (STEM) side-views of pristine and implanted NT arrays. Upon implantation, the NT height reduces due to bending, sputtering and densification. On top of the NT the blurred white platinum capping layer is visible, the gray bottom layer depicts the underlying titanium foil.

calculations, and analytical treatment to elucidate compositional patterning upon low-energy ion implantation of titania NT with carbon ions at low fluences. The prominent NT geometry with a confined material volume and distinct boundaries and interfaces plays a key role for pattern formation. First, we present and discuss our experimental results by considering the partly contrary irradiation effects of sputtering versus readsorption and plastic flow as well as amorphization versus crystallization. Second, we discuss these findings within the framework of driven alloys that is able to account for the results based on DFT predictions of the enthalpies of mixing. In this way, we connect the occurrence of compositional patterns at such low ion energies and ion fluences to the unique NT structure.

2. Results and Discussion

2.1. Implantation Effects in Titania Nanotube Arrays

We implanted titania nanotube (NT) arrays with ^{12}C ions with two different energies: 60 keV yielded more sub-surface defects, followed by 150 keV to ensure higher penetration depths ranging up to the underlying titanium foil. In detail, stooping and range of ions in matter (SRIM) simulations^[22] with carefully chosen effective material densities depicted in Figure S1, Supporting Information show ion ranges of 453.9 nm with a straggle of 148.9 nm at 60 keV ion energy, resulting in an implantation of the upper half of the NT arrays. Hence, the combination of both ion energies 60 keV followed by 150 keV, as used in our study, resulted in a more uniform implantation profile of the entire NT arrays with average ion ranges of 743.7 nm and a straggle of 354.5 nm.

As depicted in scanning transmission electron microscopy (STEM) side views in **Figure 1**, the morphology of NT arrays changes upon implantation. In general, the pristine NT arrays show a bamboo-like structure, due to the water content of the electrolyte small ripples are formed on the side walls.^[23] During

anodization, NTs grow perpendicular to the underlying titanium foil with heights in the range of 1000 to 1800 nm (the complete lamella is depicted in Supporting Information).

Carbon (C) implantation with 60 keV followed by 150 keV with a fluence of 1×10^{16} ions cm^{-2} each, induces a slight bending in the upper parts near the surface and an increased bending of the lower parts of the NT. It is correlated with the region of maximum defect density of the implanted ions, estimated with SRIM simulations (see Figure S1, Supporting Information). As a consequence of ionic/atomic recoils, ballistic collision cascades result in a contribution to energy loss (see Figure S2, Supporting Information). Since the density of energetic recoil atoms is highest for surface-near implantation achieved by 60 keV ions, we propose a considerable local effective temperature increase in the upper parts of the NT arrays and relaxation due to capillarity-driven viscous material flow.^[24] Yet, the overall temperature stays well below the melting point of TiO_2 . Thus, the plastic flow is mediated by creation and relaxation of implantation induced defects (see Supporting Information for details). Due to the confined NT volume, we also assume an impeded heat transport compared to bulk materials. A second local maximum of the recoil atom distribution resulting from 150 keV ion implantation near the titanium foil superimposes the 60 keV maximum, resulting in increased bending of the lower parts of the NT and an effective shrinkage of the average array height to 566 ± 19 nm.

We assume that NT shrinkage is caused by both radiation-induced viscous material flow mentioned above, and by sputtering effects within the NT. The former effect is driven by stresses generated during self-organized growth, as well as capillarity. Hence, upon ion implantation, not only the closure of tubes on the surface and a thickening of the NT walls is observed, but also, the complete titania layer relaxes and shrinks. The latter effect of sputtering is amplified within the NT layer since the incoming ion flux hinders the sputtered material from escaping the NT: instead it readsorbs on opposing side walls or deeper inside the NT.^[24] In this way, we propose that the combination of sputtering and the readsorption of

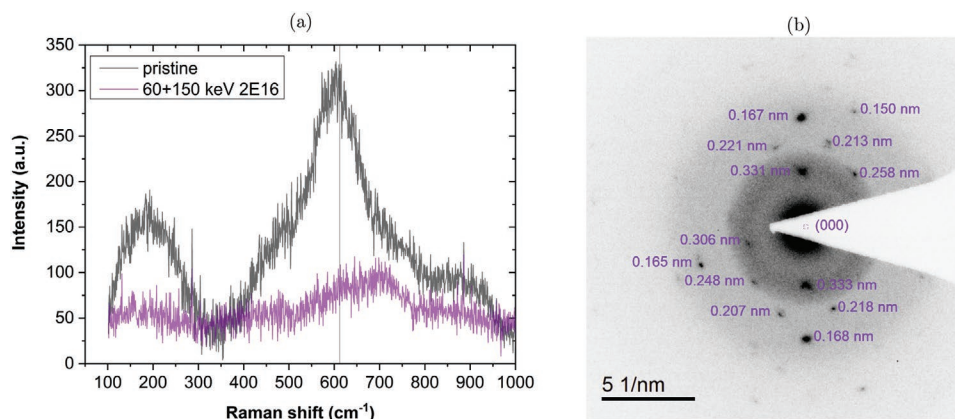


Figure 2. a) Raman spectra of pristine and C implanted NT arrays. The reference line indicates the rutile 612 cm^{-1} peak. b) Inverted selected area electron diffraction (SAED) pattern obtained from NT implanted with 60 keV followed by 150 keV and a fluence of 1×10^{16} ions cm^{-2} each, showing blurred diffraction rings and distinct reflexes. The diffraction rings indicate the amorphous TiO_2 phases, while the characteristic distances of the reflexes from the center of diffraction fit closest to rutile TiO_2 literature values (see Table S1, Supporting Information).

transmitted ions with lower kinetic energy also leads to thickening of the walls, which is displayed by a softening of the intrinsically clearly-defined boundaries of the single NT.

In the present case, the prominent NT geometry leads to a confined material volume with distinct boundaries and interfaces. Assuming an average NT wall thickness of 30 nm and the 7° standard tilt angle of the ion beam, we deduce that an ion incident on a boundary of the NT can cross a NT wall with a straight path after 244.3 nm and leave the NT. In this simplified picture, deflection and scattering effects are neglected. However, one ion might penetrate two or three NTs and cause sputtering within the NT arrays. On the inner NT surfaces, the sputtering yield is fairly higher than on the uppermost surface, since the ion incident angle approaches the sputtering yield maximum at about $70^\circ\text{--}80^\circ$.^[25] In addition, decelerated ions with lower energies might not cross single NTs, but might be deflected at the NT boundary. Furthermore, the confined material volume spatially changes the formation of collision cascades. Large displacement cascades can only develop along the growth direction of the NT toward the uppermost surface or the bottom of the NT arrays. In plane, the cascade lengths are limited due to the inner NT boundaries, namely a maximum distance of 30–50 nm. Since the lateral straggle of defects is assumed to be at least twice this distance, (up to 150 nm for combined implantation of 60 keV followed by 150 keV, obtained by SRIM simulations, see Supporting Information), the transmission of recoils is anticipated. Thus, recoil ions will escape the inner NT surfaces and reabsorb either on the opposing NT wall segments, or, as result of the incoming ion flux when compared to bulk material, deeper within the NT. In addition, sub-cascade formation is expected, as the implantation energy of C is above typical threshold energies and the scattering cross-section of C is comparably small (see Supporting Information). Hence, we propose the superposition of cascade effects in the confined NT volume (defects comparable to displacements, relocalizations, vacancies, and interstitials in crystalline materials) within the NT walls. Consequently, even a low C fluence can have large effects on the NT arrays when compared to bulk materials.

2.2. Formation of Rutile Crystallites

In order to determine the bond characteristics of the X-ray diffraction (XRD)-amorphous titania NT arrays (see grazing incidence X-ray diffraction measurements, Figure S4, Supporting Information), we employed Raman spectroscopy. As depicted in Figure 2a, pristine arrays show one distinct broad peak at about 612 cm^{-1} , indicating the A_{1g} mode of a rutile TiO_2 polymorph with nanocrystallites.^[26,27] Additionally, a broad peak congruent with the B_{1g} mode at 143 cm^{-1} was observed.^[26] Upon C implantation with 60 keV followed by 150 keV with a fluence of 1×10^{16} ions cm^{-2} each, the peak vanishes. Other peaks related to rutile TiO_2 cannot be distinguished from the fluorescent background, but also cannot be excluded. In fact, the NT array color changes to darker shades upon implantation.^[28] Also, as stated above, the film thickness decreases. To ensure that the nanostructures are not deformed, only small laser intensities were employed.^[29] Thus, on one hand, an increase of the fluorescent signal in the range of $100\text{--}800\text{ cm}^{-1}$ is detected.^[30] On the other hand, with lower laser intensities the penetration depths also decrease in a way such that mainly surface near regions account for the Raman signal.

In contrast, selected area electron diffraction (SAED) pattern obtained from the whole NT layer show crystalline patterns for C implanted NT arrays. For pristine NT arrays, no such patterns, only ambiguous diffraction rings stemming from the amorphous phase were detected (not shown here). In Figure 2b the inverted diffraction pattern of C implanted NT arrays is depicted. It reveals diffraction rings, as expected from samples with small crystallites in the nm range, as well as a pronounced point diffraction pattern. We associate the characteristic distances of the points of the diffraction pattern with rutile TiO_2 , since they resemble standard literature values (see Supporting Information).^[31,32]

Hence, the combined results of Raman spectroscopy and SAED indicate that the initially small rutile TiO_2 nanocrystallites in pristine NT arrays grow upon C implantation to fairly larger crystallites, producing the observed diffraction patterns. Due to compositional patterning of C and O described below,

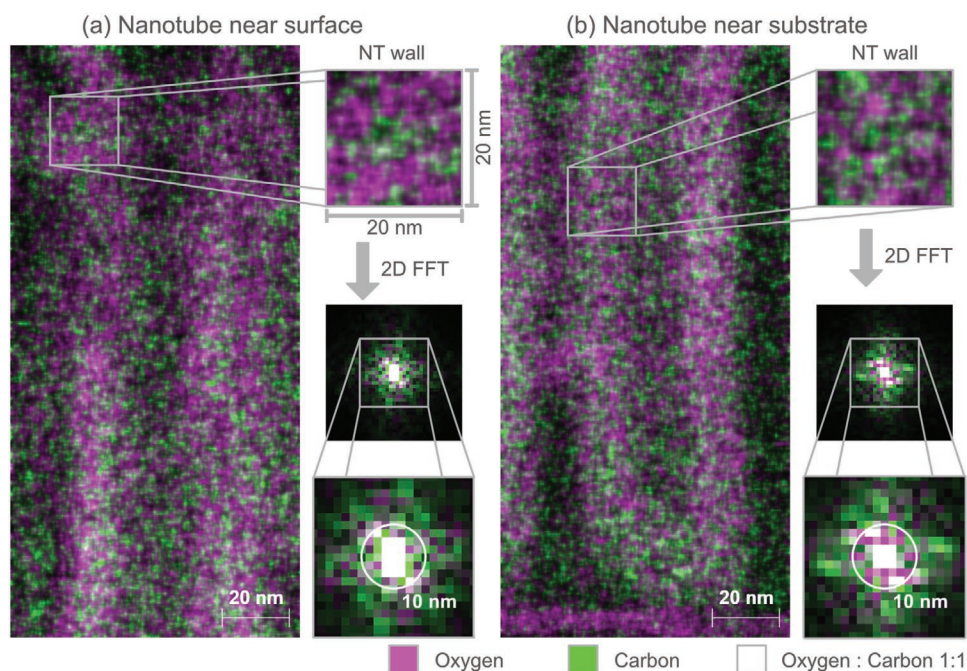


Figure 3. Overlay of energy-dispersive X-ray spectroscopy of scanning transmission electron microscopy (STEM-EDX) images of the oxygen (magenta) and carbon (green) channel of C implanted NT arrays a) near the surface and b) near the substrate. To analyze the characteristic sizes of distinct domains qualitatively, detailed images in the size of 20 nm × 20 nm of the NT walls were obtained and 2D FFT was carried out. The highlighted circles show the frequency related to domain sizes of 10 nm.

pure O domains binding to Ti might promote the growth of rutile crystallites. In addition, the preferential sputtering of O might lead to oxygen (O)-depleted regions (within the NT)^[33] connected to the formation of Ti^{3+} species, as well as O-rich regions at the inner NT boundaries, where sputtered O re-adsorbs. O-depleted regions are favorable for rutile crystal formation, as observed for anatase nanoparticles under visible light.^[27] These processes are further promoted by the enhanced irradiation-induced defect-density, and correspondingly, higher effective temperatures due to the confined NT volume. Hence, ion implantation and the specific NT geometry serve advantageous conditions for rutile crystal formation.

2.3. Compositional Patterning - Experiments

High-resolution element mappings obtained by energy-dispersive X-ray spectroscopy of STEM measurements (STEM-EDX) show a change of the O distribution within the NT arrays upon implantation. High-angle annular dark-field (HAADF) images and original STEM-EDX maps of surface-near and substrate-near regions of the NT are depicted in Figures S6 and S7, Supporting Information, respectively. In **Figure 3**, the overlay of O and C atoms is depicted for C implanted NT arrays. For pristine NT arrays, see **Figure S5**, Supporting Information, we observe a rather uniform distribution of O and only marginal traces of C within surface-near regions. Hence, corresponding overlays of C-O, O-F, and C-F do not show any signs of phase separation. In contrast, for C implanted NT the zoom-in images in **Figure 3** reveal a phase separation, since distinct domains with increased C concentration separate from other domains with increased

O concentration. Evidently, the C-O-subsystem decomposes upon C implantation. Signs of spherical nucleation spots with a very clear interphase and completely random distribution, as observed in classical nucleation, are not present.^[34]

Occurrence of concentration modulations appears in regions with high energy loss, that is, nuclear loss (in terms of defect generation) and electronic loss. As stated above, 60 keV ions dissipate most of their energy in surface-near regions. Ions with 150 keV show larger ranges causing more defects near the substrate, but also energy loss near the surface. Hence, the combination of both implantation energies will lead to a higher degree due to the accumulated effects. In fact, the C-O-overlays of energy loss in **Figure 3a,b** corroborate this assumption qualitatively, since the C domains appear larger in surface-near regions in **Figure 3a**. In contrast, in **Figure 3b**, the domains occur smaller, the NT appears more heterogeneous. Thus, the degree of patterning is directly connected to the implanted fluence and ion energy. The related 2D fast Fourier transformation (FFT) overlays of C and O support presence of a very regular compositional pattern. The center of the FFT plots corresponds to low frequencies and large domain sizes. Near the surface of the NT **Figure 3a**, we observe a large white central area corresponding to an equal abundance of large C and O domains. Moving radially outward, green C domains dominate the spectrum. At 10 nm domain sizes, spatially separated C and O domains are apparent. In contrast, near the substrate in **Figure 3b**, magenta O dominates regions adjacent to the white center with the equal abundance. Hence, O domains are noticeably larger than C domains occurring radially outward.

In **Figures S10** and **S11**, Supporting Information, the element-specific FFT spectra of the single NT walls shown in

Table 1. Dilute limit enthalpies of mixing, ϵ , and κ in the framework of the regular solution model, as determined by density functional theory (DFT) calculations. Ensemble averages of 16 different configurations were employed for bulk (index b) and surface (index s) properties, respectively. The standard deviation given for ϵ primarily reflects intrinsic fluctuations due to doping amorphous cells.

System	ϵ_b [eV]	κ_b [eV]	ϵ_s [eV]	κ_s [eV]
TiO ₂ /C	1.77 ± 0.82	0.196	2.58 ± 0.97	0.170
TiO ₂ /F	-0.183 ± 0.304	1.23	-0.44 ± 0.56	1.15

Figures S6 and S7, Supporting Information are depicted. Apparently, the peaks describing the characteristic domain sizes are the first local maxima next to the peaks stemming from image boundaries. When the C domain sizes are quantified, a size ranging from 9.4–10.45 nm, for both surface-near and substrate-near regions, is obtained. Similarly, the size of the O domains measure 9.1–9.77 nm, independently of the location. Despite their substantial similarity, these domain sizes obtained with FFT resemble the qualitative results observed by EDX-STEM.

In contrast, the fluorine (F)-O subsystem does not show comparable signs of compositional patterning. In Figures S8 and S9, Supporting Information, the elemental STEM-EDX overlays depict the rather point-wise distribution of F without forming distinct domains, as observed for the C-O subsystem. Also, the F-O 2D FFT overlays illustrate a wider extension, hence a more heterogeneous elemental distribution. The C-F subsystem is only slightly correlated since C and F are complementary substitutes of O.

2.4. Compositional Patterning - Ab Initio Based Thermodynamic Considerations

Our experiments clearly indicate occurrence of a periodic compositional pattern of C-rich and C-depleted regions, which arises spontaneously during implantation of C into titania NT and appears to be stationary, viz. lacks coarsening for the doses investigated. Previous work by Enrique et al.^[35] based on Martin's concept of "driven alloys"^[36] has shown that stationary compositional patterns can be dynamically stabilized by competing processes that act on different length scales. In the present environment, ion implantation induced ballistic mixing is understood as compositionally randomizing process that drives the system out of equilibrium, while relaxation processes tend to restore it and act on a shorter length scale; it is the interplay of these two processes which we suspect to be responsible for regular pattern formation.

For the present work we consider C and F doped TiO₂ while noting that C and F have a comparable atomic radius to O (e.g., van der Waals radius^[37] $r_O = 1.5 \text{ \AA}$, $r_C = 1.77 \text{ \AA}$, $r_F = 1.56 \text{ \AA}$), while Ti atoms are of much larger size ($r_{Ti} = 2.46 \text{ \AA}$). From these simple considerations, we expect that C and F dopants preferentially occupy O sites, i.e. that the C-O and C-F subsystems constitute a "substitutional alloy". This notion is directly corroborated by our high resolution STEM-EDX measurements (Figure 3) that indicate an increase of the C content at the cost of O content, while the Ti content proves to be largely

uncorrelated. Based on these facts, the regular solution model (e.g., ref. [38]) applied to O sites promises to be a suitable framework to approximately treat thermodynamics in the presence of dopants. Here, $\epsilon = \epsilon_{AB} - \frac{1}{2}(\epsilon_{AA} + \epsilon_{BB})$ with A = O and B = C or F, respectively, denotes the enthalpy of mixing, i.e. enthalpy difference between a perfectly mixed TiAB solid solution and the average pure systems (TiA₂ and TiB₂, respectively); $\kappa = \frac{1}{2}(\epsilon_{BB} - \epsilon_{AA})$ is defined accordingly.

DFT based total energy calculations with the techniques described in Section 4 were conducted to predict the parameters ϵ and κ from first principles (see Table 1). Clearly, only the TiO₂/C system reveals a positive heat of mixing, while TiO₂/F prefers the mixed state for enthalpic (and, of course, also entropic) reasons. As the surface does not reveal any qualitative differences regarding these aspects and negligible tendencies for surface segregation, (Table 1) we will focus on the bulk in the following.

We continue by choosing the spatially varying atomic dopant concentration, $\Phi(\vec{r})$, as order parameter. Following Cahn and Hilliard,^[39] the free enthalpy density $g(\vec{r})$ is then given by the sum of the volume and interface contributions

$$g(\vec{r}) = g_v(\vec{r}) + g_i(\vec{r}) \quad \text{with} \quad (1)$$

$$g_v(\vec{r}) = \frac{\epsilon}{\xi^3} \Phi(\vec{r})(1 - \Phi(\vec{r})) + \frac{\kappa}{\xi^3} \Phi(\vec{r}) + \frac{kT}{\xi^3} (\Phi(\vec{r}) \ln \Phi(\vec{r}) + (1 - \Phi(\vec{r})) \ln (1 - \Phi(\vec{r}))) \quad (2)$$

$$g_i(\vec{r}) = \frac{1}{2} \Gamma (\nabla \Phi(\vec{r}))^2 \quad (3)$$

The quantity

$$\Gamma = \frac{2\epsilon}{v\xi} \quad (4)$$

parameterizes the interface enthalpy that is present for spatially varying order parameters, where v denotes the number of atomic neighbors for an O site. We proceed by assuming that O has on average $v \approx 3$ neighbors, (as in the crystalline polymorphs) and estimating the "effective lattice parameter," $\xi \approx 2.62 \text{ \AA}$, by formally assigning the total cell volume to the O atoms only, and then equating ξ^3 to the cell volume per O atom.

Employing "Model B" dynamics,^[40] supplemented by a ballistic relocation term with relocation length, L_b , we follow Enrique et al.^[35] in performing a linear stability analysis around a stable configuration, which presently yields for the amplification factor

$$\frac{w(k)}{M} = -\Gamma k^4 - g_v''(\Phi_0) k^2 - \gamma (1 - \hat{w}_{L_b}(k)) \quad (5)$$

where Φ_0 , γ and $\hat{w}_{L_b}(k) = \text{Atan}(kL_b)/(kL_b)$ denote the (spatially average) starting concentration, the ballistic exchange

rate normalized to mobility M and the Fourier transform of the normalized relocation distribution with relocation length L_b , respectively. The latter we derived from the representation in real space, $w_{L_b}(\vec{r}) = w_{L_b}(r) = \exp(-r/L_b)/(4\pi L_b r^2)$, which accounts for the exponential decay observed in SRIM simulations (shown in Supporting Information). Within this scope it is worth noting, that modes with $w(k) > 0$ and $w(k) < 0$ grow and vanish with time.

As for mobility, liquid-like diffusion is established to occur in glasses above the critical temperature of the mode coupling theory^[41] ($T_C \approx 1492$ K for TiO_2 ^[42]), which is reached for some tens of picoseconds in thermal spikes^[43] that arise in a delocalized manner in different spots of the collision cascade due to energy dissipation.^[42] Despite lower temperatures than T_C , flow still prevails outside these thermal spikes due to point defects, which are introduced into the amorphous matrix due to the collision cascade and constitute shear instabilities, that is radiation induced “shear transformation zones” (STZ).^[44,45] In fact, as we will demonstrate elsewhere in detail,^[24] point defect mediated viscous flow occurs in TiO_2 for temperatures as low as 10 K and also constitutes one of the key ingredients to understand pore closure observed when implanting NT arrays.

In the following, we will assume for a moment that the “melt” within a thermal spike is composed of an aggregation of shear instabilities, very much similar to point defect induced shear instabilities in the glass. Justification for this assumption stems from the observation that radiation induced viscous flow perfectly scales with the defect production rate due to ion implantation.^[24,44] That being said, we proceed by assuming that each shear instability is capable of equilibrating a certain surrounding volume to a degree determined by its inherent fluidity (typically within the range of the next nearest neighbor shell of the defect). We therefore proceed by (roughly) approximating the diffusivity of C in these regions using the Stokes–Einstein relation $D = e \cdot k T_C / (6\pi\eta r_C)$, where $1/\eta$ and r_C denote the (greatly temperature independent) global radiation induced fluidity and C atomic radius, respectively, while Euler’s number e is employed here to account for overlapping STZs (to transfer fluidity from global to local). Note, that we employ T_C here as estimate for the local temperature during a shear event in the sense that it corresponds to the communal entropy. Measuring time in damage events, namely displacements per atom (dpa), and merging things together yields

$$\gamma = 6\pi\eta r_C / (e \cdot \xi^3) \quad (6)$$

For the average experimental C concentration after implantation, $\Phi_0 \approx 0.07$, we obtain a “band” of growing modes (see Figure 4), that stabilizes length scales $\lesssim 47$ Å for compositional patterning, assuming an enhanced relocation length ($L_b = 17$ Å) due to porosity. For bulk samples ($L_b \approx 4.5$ Å) on the other hand the length scale of the patterns is not limited, i.e. dynamical size stabilization is not taking place (but occurrence of a particular domain size is expected by the fastest growing mode). Regarding the exact “numbers” concerning length scale we would like to issue a caveat here – they certainly depend on the exact choice of the parameters (ξ , for example), which we did not “tune” for agreement with experiments, but estimated from first principles and based on our physical picture regarding

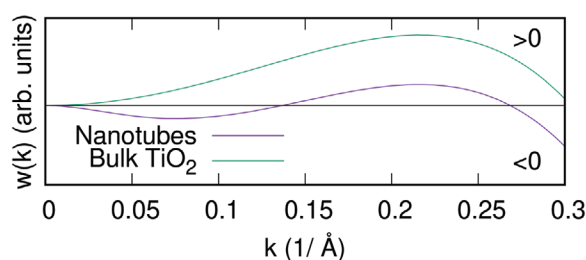


Figure 4. Amplification factor (Equation (5)), calculated for bulk titania $L_b = 4.5$ Å (Supporting Information) and a porous NT structure assuming $L_b = 17$ Å (this corresponds to densities of $4.12^{[42]}$ and 1.09 g cm^{−3} – Section 4). The latter indicates dynamic size stabilization of compositional patterns in NT arrays, while growth is unlimited in size for bulk samples.

the correct “order of magnitude”. While this is in accord with our experiments, we would again highlight the key finding: Our calculations suggest that porous morphology of NT arrays promotes occurrence of stationary compositional patterning by increasing relocation lengths relative to bulk titania; for that reason the scenario of compositional pattern presumably has not been observed in bulk titania to our knowledge. Beyond our model, the finite dimensions of the tube walls are expected to additionally limit pattern growth geometrically, once the compositional domains attain a comparable size. It is also interesting within this scope that plastic deformation during NT shrinking^[24] might constitute an additional contribution to further enhance L_b , as established during studies on severe plastic deformation.^[46] As for comparison with other materials systems, it is relevant to note that for 1.8 MeV Kr⁺ irradiation of the crystalline metallic Cu–W alloy, which reveals a comparable immiscibility as TiO_2/C , phase separation has been observed and discussed in terms of agglomeration–coagulation process within thermal spike.^[47]

2.5. Electrical Properties and Potential Applications

Connected to the local changes of the elemental distribution by compositional patterning shown in Section 2.3, we propose a modification of both local and global electrical properties. In the first attempt, we performed standard current–voltage measurements on larger areas, as specified in the Supporting Information. Indeed, we observe a considerable increase of conductivity upon C implantation: an ion energy of 60 keV with a fluence of 1×10^{16} ions cm^{−2} results in three orders of magnitude higher conductivity compared to pristine NT. On a local scale, we also obtain a comparable increase of currents measured by tunneling atomic force microscopy (TUNA). Here, the TUNA currents increase at least three orders of magnitude, from range of a few fA to more than 100 pA. Presumably, the conductivity of the NT arrays considered in this study is even higher. In fact, the local arrangement of conductive spots might resemble the compositional patterns, shown in Figure S12, Supporting Information.

Consequently, various potential applications can be anticipated: smart biosensors might detect the local adsorption of molecules or cells, due to the high biocompatibility of the arrays.^[7,48] Electrically stimulating NT scaffolds might enhance

the culture of nerve tissues.^[6,8] Further annealing might give rise to favorable photocatalytic or water splitting characteristics.^[18,49] Also, the use of masks allows a local implantation environment and, hence, enables the precise production of localized conductive areas.

3. Conclusion

In conclusion, we elucidate the drastic effects of low-energy ion implantation on titania nanotubes: the implantation of low carbon fluences results in a decrease of the height of the arrays mainly by sputtering and readsorption effects within the nanotubes, as well as capillarity-driven radiation-induced flow. Rutile nanocrystallites grow despite an expected amorphization, and, most prominent, we describe a compositional patterning of carbon and oxygen. We illustrate the distinct patterns using energy-dispersive X-ray spectroscopy maps and derive the characteristic pattern size by employing 2D fast Fourier transforms (FFTs). To reveal the underlying physics, we employ a linear stability analysis within the framework of the Cahn-Hilliard equations/Model B dynamics, supplemented by a ballistic mixing term, as proposed by Enrique et al. We show the trend of energetically more favorable phase separation of carbon and oxygen by choosing mixing enthalpies for the two limits TiO_2/C and TiO_2/F obtained by DFT calculations within amorphous TiO_2 cells. In this way, the experimentally observed characteristic pattern size is excellently resembled by our theoretical approach. Thus, ion implantation provides a particularly powerful and adjustable tool for manipulating the local element distribution of nanostructures. Consequently, also electrical, optical, and photocatalytic characteristics can be specifically tuned locally or globally to provide new functional materials with enormous surface areas.

4. Experimental Section

TiO₂ Nanotube Arrays: TiO_2 nanotube arrays were grown in a self-organization process by electrochemical anodization at room temperature. Therefore, a titanium foil (Advent Research Materials Ltd, 0.1 mm thickness, 99.6 + % purity), ultra-sonicated for 10 min each with distilled water and isopropyl alcohol, was anodized in an organic electrolyte consisting of ethylene glycol (Carl Roth GmbH & Co. KG, for synthesis), 2 vol% distilled water and 0.6 wt% ammonium fluoride (MERCK EMSUREACS). The anode was separated by a distance of 45 mm from the cathode, a platinum mesh. Applying an anodization voltage of 70 V for 6 min results in the formation of free standing nanotube (NT) arrays on the titanium foil. Finally, NT arrays were stored overnight in ethylene glycol. To remove electrolyte residues, the arrays were sonicated for 10 min in distilled water.

Ion Implantation: Mass separated ^{12}C ions were implanted using an IMC-200 ion implanter (Ion Beam Services, France) with a 7° standard tilt angle to prevent channeling effects. Using an acceleration energy of 60 keV, sub-surface implantation profiles were achieved. With higher acceleration energies of 150 keV, implanted ions and subsequently also defects deeper in the material were provided. The combination of ion energies of 60 keV followed by 150 keV with a fluence of 1×10^{16} ions cm^{-2} each yielded a more continuous profile of implanted ions to ensure a reasonably uniform ion distribution in the entire NT layer. Due to the low ion energies and fluence, as well as the cooling function of the massive substrate holder, the ion energy deposition during implantation was kept fairly low, such that substrate heating was restricted to 50 °C or less.

The stopping powers, ion ranges, and relocations of the NT material during implantation were simulated using SRIM.^[22] In order to gain more realistic results, a reduced density of 1.09 g cm^{-3} measured by X-ray reflectometry (Seifert XRD 3003 PTS, $\text{CuK}\alpha_1$ -line) as well as a chemical composition of 27.59 at% titanium (Ti), 55.17 at% oxygen (O), 6.90 at% carbon (C), and 10.34 at% fluorine (F) obtained with energy dispersive X-ray spectroscopy (Bruker) were considered.

Raman Spectroscopy: Raman measurements were carried out using a Horiba LabRam HR Evolution spectrometer (Horiba GmbH) equipped with a 473 nm laser and an Olympus MPlan N 100×/0.90 objective. To diminish a further modification of the arrays, only 1% laser intensity (corresponding to 0.12 mW on the surface) was applied. A measurement range of 100–1000 cm^{-1} was chosen with a resolution of 0.5 cm^{-1} (1800 l mm^{-1} grid). The spectra were background corrected using a self-written Python script (SciPy Library, “scipy.optimize.curve_fit”).

Transmission Electron Microscopy: For TEM measurements, an atomic resolution Cs-corrected FEI Titan3 G2 60-300 microscope was used. Prior to the preparation of a cross-sectional specimen (lamella), a platinum capping layer was sputtered with a sample tilt of 75° in 100% argon atmosphere. The capping layer was on average 65 nm thick, covered the surface completely and prevented the entering of further deposited platinum into the NT. In this way, the uppermost surface layers could be resolved by TEM.

In detail, the lamella was cut in a stepwise procedure using a Zeiss Auriga dual-beam focused ion beam instrument described by Lotnyk et al.^[50] In our case, the following milling parameter were used: both the front-side and back-side were milled using a high energy Ga-beam with 30 keV (240 pA beam current) and 15 keV (250 pA). Subsequently, the lamella was thinned with a low-energy Ga-beam for 1 min with 5 keV (20 pA) and 2 min with 2 keV (20 pA) to a thickness of 180–340 nm, depending on the sample characteristics. In order to achieve a thin lamella of about 30 nm thickness, specimens were polished with a Fischione NanoMill with low-energetic argon ions. Further cleaning was provided by a 10 min plasma treatment using a Gatan Solarus H_2/O_2 plasma cleaner.

TEM was used to study the inner morphology and texture of pristine and implanted NT arrays. The structural changes of the complete arrays upon implantation were evaluated by STEM with lower magnifications with an HAADF detector using annular ranges of 80–200 mrad. In order to determine the crystallinity of NT, SAED measurements were carried out using a Gatan US1000XP P CCD camera. In this way, diffraction patterns of surface-near regions, regions in the middle of the NT layer and the substrate were measured. The diffraction patterns were fitted using Gatan Microscopy Suite Software combined with DiffTools.^[31] Characteristic distances of reflexes were measured and compared to crystallographic literature values. STEM equipped with FEI Super-X energy dispersive X-ray (EDX) detectors and a probe forming aperture of 20 mrad yielded high-resolution element mappings for a discrete chemical analysis. The beam currents were set to 300 pA during the EDX mapping. For a more detailed analysis, quadratic zoom-in images of 20 nm side length were extracted and 2D FFT mappings were derived using Gwyddion.^[51] Comparatively, both zoom-in EDX maps and 2D FFT mappings were overlaid.

Density Functional Theory Based Calculations: Amorphous TiO_2 cells composed of 96 atoms total were prepared by quenching from the liquid (6000 K) down to 0 K with a rate of 1 K ps^{-1} using classical molecular dynamics (MD) simulations with the empirical potential due to Matsui and Akaogi^[52] as implemented in a group maintained code.^[45] In doing so, temperature and pressure were controlled with Berendsen type of thermo- and barostates,^[53] respectively, while forces were calculated using a method proposed by Wolf et al.^[54] with a cutoff of 9 Å. The cells were subsequently relaxed toward minimum ionic forces and cell stresses, respectively, using DFT^[55] ground state total energy calculations, as implemented in plane wave code, *pwscf*.^[56,57] The projector-augmented wave (PAW)^[58,59] method^[60] was employed and the exchange correlations were treated within the Perdew, Burke, Ernzerhof parameterization of the generalized gradient approximation.^[61] Ti on-site 3d-electron-electron interactions were treated within the Hubbard model using the DFT+U approach^[62,63] with $U = 4.2$ eV as demonstrated in previous studies (ref. [64] and references therein). Systematic

convergence tests yielded a plane wave cutoff and Monkhorst–Pack k -point mesh^[65] as large and dense as 707.5 eV and $2 \times 2 \times 2$, respectively, which proved to be sufficient.

To determine the dilute-limit enthalpies of mixing a single O atom was randomly replaced per cell with C and F, respectively, followed by a relaxation of the ionic and cell degrees of freedom toward minimum forces and stresses, respectively. As the obtained values vary from site to site due to the amorphous nature of the cells, this procedure was repeated until average dilute-limit enthalpies of mixing of sufficient accuracy were obtained. Surface enthalpies were calculated by utilizing supercells, composed of relaxed volume cells supplemented by vacuum layers in the $\pm z$ directions, twice the linear dimensions of the initial volume cells, that were subsequently relaxed toward minimum ionic forces at fixed cell dimensions. Correspondingly, dilute surface enthalpies of mixing were obtained by randomly replacing the outermost O surface atoms by C or F, respectively, and again relaxing the ionic degrees of freedom toward minimum forces.

- Filename: Detailed SRIM simulations of carbon implantation, SEM images of TEM lamellas, GID measurements of pristine, and carbon implanted NT, literature values for d -spacings of rutile and anatase TiO₂, EDX-STEM images, and 2D FFTs of pristine and carbon implanted NT in surface-near and substrate-near regions, FFT spectra of single carbon implanted NT in surface-near and substrate-near regions, theoretical considerations on ballistic diffusion (PDF).

Supporting Information

Supporting Information is available from the Wiley Online Library or from the author.

Acknowledgements

The authors gratefully acknowledge A. Mill for the preparation of TEM lamella, M. Mensing for discussions regarding SAED measurements, J. Lehnert for Raman measurements, P. Schlupp for current–voltage measurements, and C. Steele for proofreading. This project was funded in parts by a scholarship of the Heinrich Böll foundation and the German Ministry of Science and Education (BMBF), project EYECULTURE, FKZ 161A574C/031A574C. Partly, the project was performed within the Leipzig Graduate School of Natural Sciences, Building with Molecules and Nano Objects (BuildMoNa).

Open access funding enabled and organized by Projekt DEAL.

Conflict of Interest

The authors declare no conflict of interest.

Data Availability Statement

The data that support the findings of this study are available from the corresponding author upon reasonable request.

Keywords

density functional theory calculations, driven alloys, mixing enthalpies, pattern formation, phase separation, titanium dioxide, transmission electron microscopy

Received: May 5, 2021
Revised: June 11, 2021
Published online: July 3, 2021

- [1] I. Paramasivam, H. Jha, N. Liu, P. Schmuki, *Small* **2012**, *8*, 3073.
- [2] I. S. Cho, J. Choi, K. Zhang, S. J. Kim, M. J. Jeong, L. Cai, T. Park, X. Zheng, J. H. Park, *Nano Lett.* **2015**, *15*, 5709.
- [3] D. K. Roh, W. S. Chi, H. Jeon, S. J. Kim, J. H. Kim, *Adv. Funct. Mater.* **2014**, *24*, 379.
- [4] A. Roguska, A. Belcarz, J. Zalewska, M. Hołdyński, M. Andrzejczuk, M. Pisarek, G. Ginalska, *ACS Appl. Mater. Interfaces* **2018**, *10*, 17089.
- [5] P. Roy, S. Berger, P. Schmuki, *Angew. Chem., Int. Ed.* **2011**, *50*, 2904.
- [6] V. Dallacasa grande, M. Zink, S. Huth, A. Jakob, M. Müller, A. Reichenbach, J. A. Käs, S. G. Mayr, *Adv. Mater.* **2012**, *24*, 2399.
- [7] S. Kallendrusch, F. Merz, I. Bechmann, S. G. Mayr, M. Zink, *Adv. Healthcare Mater.* **2017**, *6*, 1601336.
- [8] C. Ronzani, T. Cottineau, I. Gonzalez-Valls, V. Keller, S. Picaud, N. Keller, M. J. Roux, *Adv. Funct. Mater.* **2018**, *28*, 1804639.
- [9] F. Schmidt-Stein, S. Thiemann, S. Berger, R. Hahn, P. Schmuki, *Acta Mater.* **2010**, *58*, 6317.
- [10] E. Sennik, N. Kilinc, Z. Z. Ozturk, *J. Alloys* **2014**, *616*, 89.
- [11] S. P. Albu, A. Ghicov, S. Aldabergenova, P. Drechsel, D. LeClere, G. E. Thompson, J. M. Macak, P. Schmuki, *Adv. Mater.* **2008**, *20*, 4135.
- [12] Y. Lu, J. Wang, Y. Chen, X. Zheng, H. Yao, S. Mathur, Z. Hong, *Adv. Funct. Mater.* **2021**, *31*, 2009605.
- [13] N. Khaliq, M. A. Rasheed, M. Khan, M. Maqbool, M. Ahmad, S. Karim, A. Nisar, P. Schmuki, S. O. Cho, G. Ali, *ACS Appl. Mater. Interfaces* **2021**, *13*, 3653.
- [14] N. S. Peighambardoust, S. Khameneh Asl, R. Mohammadpour, S. K. Asl, *Electrochim. Acta* **2018**, *270*, 245.
- [15] A. Ghicov, J. M. Macak, H. Tsuchiya, J. Kunze, V. Haeublein, L. Frey, P. Schmuki, *Nano Lett.* **2006**, *6*, 1080.
- [16] X. Zhou, V. Häublein, N. Liu, N. T. Nguyen, E. M. Zolnhofer, H. Tsuchiya, M. S. Killian, K. Meyer, L. Frey, P. Schmuki, *Angew. Chem., Int. Ed.* **2016**, *55*, 3763.
- [17] J. H. Park, S. Kim, A. J. Bard, *Nano Lett.* **2006**, *6*, 24.
- [18] X. Zhou, N. Liu, P. Schmuki, *ACS Catal.* **2017**, *7*, 3210.
- [19] H. Feng, Z. Xu, L. Ren, C. Liu, J. Zhuang, Z. Hu, X. Xu, J. Chen, J. Wang, W. Hao, Y. Du, S. X. Dou, *ACS Catal.* **2018**, *8*, 4288.
- [20] Y. Yang, L. C. Kao, Y. Liu, K. Sun, H. Yu, J. Guo, S. Y. H. Liou, M. R. Hoffmann, *ACS Catal.* **2018**, *8*, 4278.
- [21] X. Liu, P. Carvalho, M. N. Getz, T. Norby, A. Chatzidakis, *J. Phys. Chem. C* **2019**, *123*, 21931.
- [22] J. F. Ziegler, M. Ziegler, J. Biersack, *Nucl. Instrum. Methods Phys. Res., Sect. B* **2010**, *268*, 1818.
- [23] Y.-Y. Song, P. Schmuki, *Electrochem. Commun.* **2010**, *12*, 579.
- [24] A. Kupferer, S. Mändl, S. G. Mayr, unpublished.
- [25] Q. Wei, K.-D. Li, J. Lian, L. Wang, *J. Phys. D: Appl. Phys.* **2008**, *41*, 172002.
- [26] S. Mändl, G. Thorwarth, M. Schreck, B. Stritzker, B. Rauschenbach, *Surf. Coat. Technol.* **2000**, *125*, 84.
- [27] L. Stagi, C. M. Carbonaro, R. Corpino, D. Chiriu, P. C. Ricci, *Phys. Status Solidi B* **2014**, *252*, 124.
- [28] A. Kupferer, S. Vogt, S. Mändl, M. Grundmann, S. G. Mayr, unpublished.
- [29] H. Palneedi, J. H. Park, D. Maurya, M. Peddigari, G.-T. Hwang, V. Annareddy, J.-W. Kim, J.-J. Choi, B.-D. Hahn, S. Priya, K. J. Lee, J. Ryu, *Adv. Mater.* **2018**, *30*, 1705148.
- [30] F. Rossella, P. Galinetto, M. C. Mozzati, L. Malavasi, Y. D. Fernandez, G. Drera, L. Sangaletti, *J. Raman Spectrosc.* **2009**, *41*, 558.
- [31] D. Mitchell, *Microsc. Res. Tech.* **2008**, *71*, 588.
- [32] C. D. Valentin, G. Pacchioni, A. Selloni, *Chem. Mater.* **2005**, *17*, 6656.
- [33] J. Sullivan, S. Saied, I. Bertoti, *Vacuum* **1991**, *42*, 1203.
- [34] F. Findik, *Mater. Des.* **2012**, *42*, 131.
- [35] R. A. Enrique, P. Bellon, *Phys. Rev. Lett.* **2000**, *84*, 2885.

- [36] G. Martin, P. Bellon, *Solid State Phys.* **1996**, *50*, 189.
- [37] S. Alvarez, *Dalton Trans.* **2013**, *42*, 8617.
- [38] P. Haasen, *Physikalische Metallkunde*, Springer, Berlin, Heidelberg **2013**.
- [39] J. W. Cahn, J. E. Hilliard, *J. Chem. Phys.* **1958**, *28*, 258.
- [40] P. C. Hohenberg, B. I. Halperin, *Rev. Mod. Phys.* **1977**, *49*, 435.
- [41] W. Götze, *Complex Dynamics of Glass-Forming Liquids: A Mode-Coupling Theory*, International Series of Monographs on Physics, OUP, Oxford **2009**.
- [42] A. Holm, S. G. Mayr, *Phys. Rev. B* **2021**, *103*, 174201.
- [43] T. D. de la Rubia, R. S. Averback, R. Benedek, W. E. King, *Phys. Rev. Lett.* **1987**, *59*, 1930.
- [44] S. G. Mayr, Y. Ashkenazy, K. Albe, R. S. Averback, *Phys. Rev. Lett.* **2003**, *90*, 055505.
- [45] S. G. Mayr, *Phys. Rev. Lett.* **2006**, *97*, 195501.
- [46] N. Verma, N. Pant, J. A. Beach, J. Ivanisenko, Y. Ashkenazy, S. Dillon, P. Bellon, R. S. Averback, *Acta Mater.* **2019**, *170*, 218.
- [47] X. Zhang, J. A. Beach, M. Wang, P. Bellon, R. S. Averback, *Acta Mater.* **2016**, *120*, 46.
- [48] S. Mayazur Rahman, A. Reichenbach, M. Zink, S. G. Mayr, *Soft Matter* **2016**, *12*, 3431.
- [49] H. Zhang, J. H. Kim, J. H. Kim, J. S. Lee, *Adv. Funct. Mater.* **2017**, *27*, 1702428.
- [50] A. Lotnyk, D. Poppitz, U. Ross, J. Gerlach, F. Frost, S. Bernütz, E. Thelander, B. Rauschenbach, *Microelectron. Reliab.* **2015**, *55*, 2119.
- [51] D. Nečas, P. Klapetek, *Open Phys.* **2012**, *10*, 181.
- [52] M. Matsui, M. Akaogi, *Mol. Simul.* **1991**, *6*, 239.
- [53] H. J. C. Berendsen, J. P. M. Postma, W. F. van Gunsteren, A. DiNola, J. R. Haak, *J. Chem. Phys.* **1984**, *81*, 3684.
- [54] D. Wolf, P. Keblinski, S. R. Phillpot, J. Eggebrecht, *J. Chem. Phys.* **1999**, *110*, 8254.
- [55] W. Kohn, L. J. Sham, *Phys. Rev.* **1965**, *140*, A1133.
- [56] P. Giannozzi, S. Baroni, N. Bonini, M. Calandra, R. Car, C. Cavazzoni, D. Ceresoli, G. L. Chiarotti, M. Cococcioni, I. Dabo, A. Dal Corso, S. de Gironcoli, S. Fabris, G. Fratesi, R. Gebauer, U. Gerstmann, C. Gougousis, A. Kokalj, M. Lazzeri, L. Martin-Samos, N. Marzari, F. Mauri, R. Mazzarello, S. Paolini, A. Pasquarello, L. Paulatto, C. Sbraccia, S. Scandolo, G. Sclauzero, A. P. Seitsonen, A. Smogunov, et al., *J. Phys.: Condens. Matter* **2009**, *21*, 395502.
- [57] P. Giannozzi, O. Andreussi, T. Brumme, O. Bunau, M. B. Nardelli, M. Calandra, R. Car, C. Cavazzoni, D. Ceresoli, M. Cococcioni, N. Colonna, I. Carnimeo, A. Dal Corso, S. de Gironcoli, P. Delugas, R. A. DiStasio Jr, A. Ferretti, A. Floris, G. Fratesi, G. Fugallo, R. Gebauer, U. Gerstmann, F. Giustino, T. Gorni, J. Jia, M. Kawamura, H.-Y. Ko, A. Kokalj, E. Kkbenli, M. Lazzeri, et al., *J. Phys.: Condens. Matter* **2017**, *29*, 465901.
- [58] P. E. Blöchl, *Phys. Rev. B* **1994**, *50*, 17953.
- [59] G. Kresse, D. Joubert, *Phys. Rev. B* **1999**, *59*, 1758.
- [60] Pseudopotential files *Ti.pbe-spn-kjpaw_psl.1.0.0.UPF*, *O.pbe-n-kjpaw_psl.1.0.0.UPF*, *C.pbe-n-kjpaw_psl.1.0.0.UPF* and *F.pbe-n-kjpaw_psl.1.0.0.UPF*, <https://www.quantum-espresso.org> (accessed: November 2018).
- [61] J. P. Perdew, K. Burke, M. Ernzerhof, *Phys. Rev. Lett.* **1996**, *77*, 3865.
- [62] V. I. Anisimov, J. Zaanen, O. K. Andersen, *Phys. Rev. B* **1991**, *44*, 943.
- [63] M. Cococcioni, S. de Gironcoli, *Phys. Rev. B* **2005**, *71*, 035105.
- [64] H. H. Pham, L.-W. Wang, *Phys. Chem. Chem. Phys.* **2015**, *17*, 11908.
- [65] H. J. Monkhorst, J. D. Pack, *Phys. Rev. B* **1976**, *13*, 5188.